

Scaling Laws for Uncertainty in Deep Learning

Mattia Rosso¹ Simone Rossi² Giulio Franzese² Markus Heinonen³ Maurizio Filippone¹

Abstract

Scaling laws in deep learning describe the predictable relationship between a model’s performance, usually measured by test loss, and key design choices such as dataset and model size. Inspired by these findings, we investigate a parallel direction: do similar scaling laws govern predictive uncertainties in deep learning? Identifiable models under a Bayesian framework exhibit $O(1/N)$ epistemic uncertainty contraction rate, with respect to dataset size N . However, these guarantees fail in over-parameterized regimes, where scaling behaviors remain largely unexplored. Across vision and language tasks, we show that in- and out-of-distribution predictive uncertainties, estimated via popular Bayesian and ensemble methods, follow predictable scaling laws relative to model and dataset size. Besides the elegance of scaling laws and the practical utility of extrapolating uncertainties to larger data or models, this work provides strong evidence to dispel recurring skepticism against Bayesian approaches: “*In many applications of deep learning we have so much data available: what do we need Bayes for?*” Our findings show that “*so much data*” is typically not enough to make epistemic uncertainty negligible.

1. Introduction

Empirical *scaling laws* describe how deep learning performance improves predictably with increasing data, parameters, or compute, typically following a power-law decay

$$f(x) \propto x^\gamma, \quad \gamma < 0 \quad (1)$$

where $x \in \{N, P, C\}$ denotes dataset size, parameter count, or compute budget (Kaplan et al., 2020; Hoffmann et al.,

¹King Abdullah University of Science and Technology (KAUST), Saudi Arabia ²EURECOM, France ³Aalto University, Finland. Correspondence to: Mattia Rosso <mattia.rosso@kaust.edu.sa>.

Preprint. February 10, 2026.

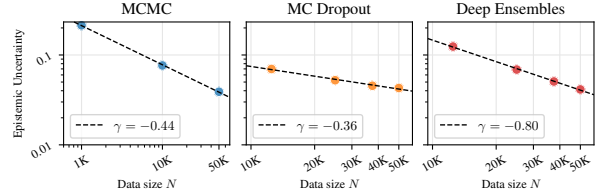


Figure 1. **Deep learning uncertainty is predictable, empirically.** ResNet-18 Epistemic Uncertainty scaling with the number of training data N on CIFAR-10.

2022). A related ‘double descent’ effect shows that increasing model capacity can surprisingly improve generalization (Belkin et al., 2019). These findings suggest that bigger models often perform better. A parallel question is: do similar scaling laws govern uncertainty in deep learning?

Bayesian Deep Learning Bayesian deep learning provides a principled framework for quantifying uncertainty in neural networks by marginalizing weights, rather than relying on point estimates, to obtain predictive uncertainties (Neal, 1996; MacKay, 1995). Recent contributions show that, under rather simple conditions, inferring only a subset of model parameters can retain the capacity to represent any predictive distribution, at a significantly lower cost (Sharma et al., 2023). The ability to produce well-calibrated predictive distributions and uncertainties is essential in decision-making and safety-critical applications, such as medical diagnosis and autonomous driving, where sound quantification of uncertainty can guide downstream choices (Papa-markou et al., 2024). However, exact Bayesian inference in large networks is intractable, which has motivated scalable approximations such as those based on the Laplace method (Ritter et al., 2018; Antoran et al., 2022), Variational Inference (VI) (Graves, 2011; Shen et al., 2024), Monte Carlo Dropout (MCD) (Gal & Ghahramani, 2016), along with (non-Bayesian) Deep Ensembles (DE) (Lakshminarayanan et al., 2017), which have proven effective and practical in obtaining sensible predictive uncertainties. Sampling-based methods, such as Stochastic Gradient Langevin Dynamics (SGLD) (Welling & Teh, 2011) and Stochastic Gradient Hamiltonian Monte Carlo (SGHMC) (Chen et al., 2014) provide scalable Markov chain Monte Carlo (MCMC) techniques for posterior inference over neural network weights. In the remainder of this paper, we will generally refer to Un-

certainty Quantification (UQ) methods to indicate Bayesian and non-Bayesian approaches designed to obtain predictive uncertainties.

Predictive Uncertainty and Scaling Despite recent criticism (Wimmer et al., 2023), current trends have focused on information-theoretic decomposition of predictive uncertainties into aleatoric and epistemic parts (Hüllermeier & Waegeman, 2021). In this work, we study how *predictive uncertainties* evolve in deep models as dataset size N and model size P grow, evaluating a range of UQ methods and architectures for both vision and language modalities. With stronger emphasis on scaling with respect to N , we systematically vary optimization settings, prior choices, stochasticity level, and inference techniques, demonstrating that different configurations exhibit a range of scaling behaviors across uncertainty metrics, but crucially all of them follow power-laws (see, e.g., Figure 1).

While classic results show $O(1/N)$ posterior-variance contraction in identifiable parametric models (Cam, 1953), over-parameterized neural networks present challenges due to singular likelihoods, non-identifiability, and non-Gaussian posteriors. We specifically study the Linearized Laplace Approximation (LLA) in Section B and confirm that, under network linearization, the posterior variance scaling asymptotically approaches the $1/N$ trend.

Although empirical scaling laws apply to test performance (Kaplan et al., 2020), a systematic understanding of how uncertainty scales with N , model size P , or computational budget is lacking. Both Bayesian and non-Bayesian UQ methods yield ensembles, with Epistemic Uncertainty (EU) reflecting prediction diversity. One of the interesting aspects of scaling laws for uncertainty is to identify when EU vanishes, indicating ensemble collapse.

Singular Learning Theory (SLT) Several theories characterize neural networks in the large-data limit. SLT models deep networks as singular statistical manifolds and shows that singularities of loss minima determine learning behavior. In particular, for Bayesian learning it predicts that the expected generalization error G_n (the expected excess loss when going from n to $n+1$ training samples) decays as $\mathbb{E}[G_n] = \frac{\lambda}{n} + o(\frac{1}{n})$, where λ is the Real Log Canonical Threshold (RLCT) (learning coefficient) (Watanabe, 2009). This last quantity governs the rate at which the generalization loss approaches the irreducible loss as n (number of training data points) grows. We derive a formal connection between the generalization error and the Total Uncertainty (TU) in the case of linear models. We believe that such a framework may help explaining the scaling behavior of uncertainty in deep models.

Other perspectives include the manifold dimensionality hy-

pothesis, linking generalization to the intrinsic dimensionality of learned representations (Ansuini et al., 2019), and mechanistic interpretability efforts explaining simple scaling phenomena via emergent internal circuits (Nanda et al., 2023).

Contributions In summary, our contributions are as follows:

(i) *Empirical study.* We provide a comprehensive evaluation of predictive uncertainties using a variety of UQ methods across different architectures, modalities, and datasets. To the best of our knowledge, this is the first study to consider scaling laws associated with any form of uncertainty in deep learning.

(ii) *Scaling patterns.* We empirically demonstrate that predictive uncertainties evaluated on in- and out-of-distribution, follow power-law trends with dataset and model size. This allows us to extrapolate to large dataset sizes and to identify data regimes where UQ approaches remain relevant to characterize the diversity of the ensemble to a given numerical precision.

(iii) *Theoretical insights.* We derive a formal connection between generalization error in SLT and TU in linear models. This novel analysis provides an interesting lead to explain the scaling laws observed in the experiments for over-parameterized models.

2. Background

2.1. Uncertainty Quantification

Predictive uncertainty refers to metrics associated with an ensemble of predictive distributions and it can be decomposed into Aleatoric Uncertainty (AU), arising from intrinsic data variability, and Epistemic Uncertainty (EU), reflecting uncertainty due to limited data or model knowledge (Hüllermeier & Waegeman, 2021).

The TU is the entropy of the mean predictive distribution:

$$\text{TU}(\mathbf{x}) = \mathbb{H} \left[\frac{1}{K} \sum_{k=1}^K p(y|\mathbf{x}, \boldsymbol{\theta}^{(k)}) \right], \quad (2)$$

where $\boldsymbol{\theta}^{(k)}$ are the model parameters of the k 'th ensemble member or stochastic pass, and $p(y|\mathbf{x}, \boldsymbol{\theta}^{(k)})$ is its predictive distribution. The irreducible uncertainty AU is the average entropy of predictions:

$$\text{AU}(\mathbf{x}) = \frac{1}{K} \sum_{k=1}^K \mathbb{H} \left[p(y|\mathbf{x}, \boldsymbol{\theta}^{(k)}) \right]. \quad (3)$$

Finally, the reducible uncertainty EU is their difference,

$$EU(\mathbf{x}) = TU(\mathbf{x}) - AU(\mathbf{x}). \quad (4)$$

In this work, we study the power-law of test predictive uncertainty, averaged over all the (fixed) test samples:

$$\frac{1}{N_{\text{test}}} \sum_{n=1}^{N_{\text{test}}} U(\mathbf{x}_n), \quad U \in \{TU, AU, EU\}. \quad (5)$$

Limitations of AU and EU While popular, these entropy-based metrics have limitations: (i) The standard decomposition of TU assumes additive separation of AU and EU, which [Wimmer et al. \(2023\)](#) argues not to hold in complex deep models, and the difficulty of disentangling them hinders their interpretability ([de Jong et al., 2025](#)); (ii) Recent works highlight EU collapse of large ensembles, leading to overly confident predictions ([Kirsch, 2024](#); [Fellaji & Pennerath, 2024](#)).

Despite these criticisms, these metrics remain useful and tractable in practice, especially when paired with typical UQ methods. Their consistency across tasks such as active learning, out-of-distribution detection and model calibration makes them valuable diagnostic tools.

2.2. Scaling Laws and Generalization

Empirical studies in deep learning have demonstrated that performance metrics scale predictably with model size, dataset size and compute. Initial findings by [Hestness et al. \(2017\)](#) and [Kaplan et al. \(2020\)](#) showed that test loss typically decreases following a power-law of the form

$$\mathcal{L}(x) = \left(\frac{x_0}{x}\right)^\alpha + \text{const.}, \quad (6)$$

where x is the resource under analysis (e.g., dataset size N , model size P , or compute budget C) and α is modality- and task-specific (x_0 is a reference constant). These relationships hold consistently across model architectures, tasks, and modalities, as empirically shown by [Henighan et al. \(2020\)](#), who demonstrated similar loss scaling for language, image, video and multimodal domains. The scaling exponents differ across domains, but the functional form of the scaling law remains stable, indicating a general underlying behavior.

Theoretical explanations of scaling behaviors are only recently emerging: for example [Sharma & Kaplan \(2022\)](#); [Bahri et al. \(2024\)](#) linked α to the intrinsic dimension and spectral properties of the data, showing how the data geometry drives the reducible portion of the loss. However,

despite these empirical and theoretical advances, a comprehensive understanding of how EU and AU scale with model and data size remain an open question. Indeed, a Bayesian perspective on uncertainty scaling laws is currently missing: it is unclear what kind of power laws uncertainty exhibits, if any. Understanding uncertainty scaling could significantly enhance the development and comprehension of Bayesian deep learning.

3. Methods

In this section, we describe the approximate Bayesian inference and ensemble methods used in our experiments. We hypothesize that if uncertainty scaling laws exist, they should emerge regardless of the UQ method.

Monte Carlo Dropout. MCD is a simple and common inference method, with connections to VI ([Gal & Ghahramani, 2016](#)). During training, standard dropout is applied, while at test time dropout masks are resampled to produce stochastic forward passes, yielding ensemble predictions. Due to its simplicity and universality, MCD is a good UQ baseline.

Gaussian Approximations. Gaussian are a common family of posterior approximations, encompassing both Laplace methods ([Ritter et al., 2018](#)) and variational inference (VI) ([Graves, 2011](#)). While Laplace relies on the local curvature of the log-posterior to define the Gaussian covariance, VI instead directly optimizes an approximate distribution to match the true posterior in the Kullback-Leibler divergence (KL) sense. Building on this line of work, we also include experiments with the Improved Variational Online Newton (IVON) optimizer ([Shen et al., 2024](#)), which unifies natural-gradient VI ([Khan & Rue, 2023](#)) with an online Newton method to achieve efficient large-scale Bayesian learning.

Markov Chain Monte Carlo. MCMC is the classic method of obtaining samples from the posterior over model parameters ([Neal, 1996](#); [MacKay, 1995](#)). Gradient-based MCMC, such as Hamiltonian Monte Carlo (HMC), are some of the most effective samplers. Mini-batch-based SGHMC ([Chen et al., 2014](#)) and Langevin dynamics ([Welling & Teh, 2011](#)) have been successfully proposed to sample from the posterior over parameters of deep neural networks of moderate size ([Tran et al., 2022](#); [Izmailov et al., 2021](#)). We consider parameter sampling with both global parameter priors and Gaussian process functional priors ([Tran et al., 2022](#)).

Deep Ensembles. DE ([Lakshminarayanan et al., 2017](#)) are a popular technique to obtain predictive uncertainties, despite lacking a fully Bayesian interpretation. Multiple networks are trained independently from different seeds and uncertainty is estimated from the ensemble of predic-

tions. DE tend to provide better uncertainty estimates and are more robust to model misspecification than MCD. We train ensembles of size $M \in \{5, 10\}$.

Partially stochastic networks. We consider partially stochastic networks where only few layers are inferred, while the rest are optimized in a standard way (Sharma et al., 2023).

4. Experiments

In this section, we provide a detailed analysis of our experimental results. We first highlight the most significant findings in the vision domain, focusing on the scaling behavior of uncertainty both in-distribution and out-of-distribution (OOD) (Section 4.1). This is complemented by an analysis of uncertainty extrapolation, detailed in Figure 15. We report an experiment in the text classification setting using a GPT-2 language model (Section 4.2). For completeness, we also include a toy experiment with a Bayesian multi-layer perceptron (MLP) (Section 4.3). Our study covers a wide range of configurations across architectures, datasets, and UQ setups, providing a comprehensive view of scaling trends.

4.1. Image classification

We use common image classification architectures of ResNet (He et al., 2016), WideResNet (Zagoruyko & Komodakis, 2016) and Vision Transformer (ViT) (Dosovitskiy et al., 2021). We report the CIFAR-10 results and part of the ImageNet32 and CIFAR-100 results in the main paper, while additional analyses are provided in Section C.

4.1.1. RESNET AND WIDERESNET

If not specified, we train these models for 400 epochs with Stochastic Gradient Descent (SGD) optimizer (momentum 0.9 and weight decay 5×10^{-4}); in some experiments we adopt a cosine annealing scheduler on the learning rate and in others we do not. See Section D for more experimental details.

Monte Carlo Dropout In ResNets, we add dropout layers after the convolutional blocks and before the fully connected layers following Kim et al. (2023). For WideResNets, we adopt the official implementation by Zagoruyko & Komodakis (2016), where dropout is applied between the two convolutional layers within each residual unit. We experiment with various dropout rates finding more expressivity in the scaling laws obtained with $p = 0.5$, especially in ResNets architectures (Gal et al., 2017). Some results are reported in Figure 1, Figure 2, and Figure 6.

Across our experiments, we observe that the EU is typically

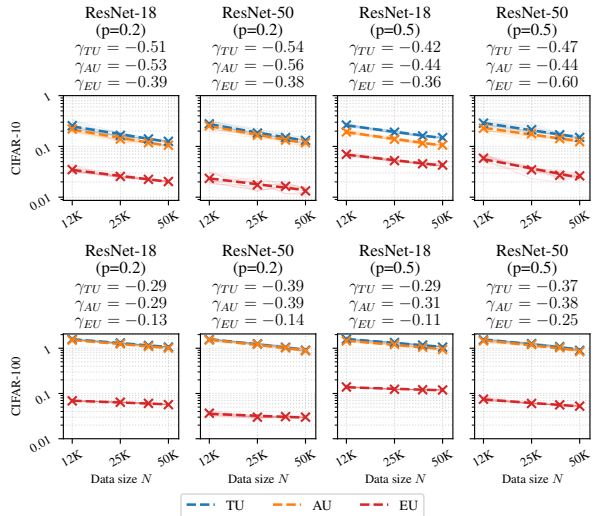


Figure 2. ResNet-d uncertainty scaling on CIFAR-10 and CIFAR-100 datasets: We use MCD (with fixed dropout rate $p = 0.2$ and $p = 0.5$); each point \times corresponds to the average over 10 independent folds (varying both data subsampling and model initialization). We consider 25%, 50%, 75% and 100% subsets of the training dataset. Dashed lines represent linear regressions fitted to the mean uncertainty metrics (AU, EU, TU) on a fixed test set (see Section 2.1), following a power-law decay of the form $N^{\gamma_{TU}}$, $N^{\gamma_{AU}}$, and $N^{\gamma_{EU}}$. Both axes are shown on a logarithmic scale.

smaller than the AU. Regarding the decreasing trend of AU that we observe across various experiments, Wimmer et al. (2023) also report that AU can decrease under limited data, making estimates potentially unreliable in such regimes. Prior work (de Jong et al., 2025; Mucsányi et al., 2024) further shows that AU and EU often correlate in image classification, suggesting entanglement in practice.

Monte Carlo Dropout combined with Sharpness Aware Minimization We also study MCD combined with SAM (Foret et al., 2020) to assess how two generalization methods interact in terms of uncertainty. We hypothesize that the increasing EU in Figure 3 arises because SAM, by avoiding sharp minima, is forced into flatter basins as $N \rightarrow \infty$: by selecting flatter basins under increased curvature, the optimizer may avoid regions of low epistemic variance and instead favor broader regions spanning more diverse functions. This aligns with recent findings that SAM can enhance ensemble diversity by trading off sharpness minimization with data-driven de-correlation (Lu et al., 2024), while MCD further promotes functional diversity via implicit bagging.

Uncertainty out-of-distribution We report results training on CIFAR-10 and testing on CIFAR-10-C (corrupted), which allows us to explore how uncertainty behaves OOD; results in Figure 4.

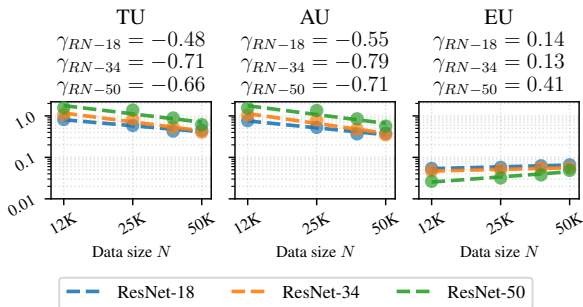


Figure 3. Impact of SGD+Sharpness Aware Minimization (SAM) on uncertainty scaling: ResNets on CIFAR-10 dataset using MCD ($p = 0.5$) for UQ. SAM biases solutions towards flatter minima and the combination with MCD preserves functional diversity as data size increases.

Deep Ensembles In Figure 5, we report scaling laws for DE (Lakshminarayanan et al., 2017), using $M \in \{5, 10\}$ independently trained models. Even for this UQ approach, we observe the emergence of power-law scalings of uncertainties with respect to the number of data.

Markov Chain Monte Carlo We also observe a similar behavior for MCMC. In these experiments, we choose a weakly informative prior over all parameters with zero mean and standard deviation of 10. In Section C, we also report results for MCMC after optimizing the priors according to the approach in (Tran et al., 2022), where we target a Gaussian process (GP) with isotropic covariance with log-length-scale of $\frac{1}{2} \log D$ and log-marginal variance of 2. In Figure 6, MCMC (1) and MCMC (2) refer to the approach of treating the first and first+second layers of the model in a stochastic fashion, while the other parameters are kept fixed to a pretrained solution (Sharma et al., 2023).

ResNets uncertainty scaling with model parameters We investigate uncertainty scaling with model size in a preliminary experiment using MCD and the IVON optimizer. IVON shows the expected increase in EU with larger models, whereas MCD does not, likely reflecting limitations of the inference scheme. Parameter permutation symmetries (e.g., swapping hidden units or attention heads) generate exponentially many modes that yield the same function. Recent works (Rossi et al., 2023; Laurent et al., 2023; Gelberg et al., 2024) show these modes are connected by low-loss paths and are not functionally distinct. Thus, increasing model capacity adds redundancy rather than distinct hypotheses, explaining the weak or flat EU dependence observed in Figure 7.

4.1.2. VISION TRANSFORMER

We explore uncertainty scaling trends using Vision Transformer (ViT) architectures (Dosovitskiy et al., 2021). We

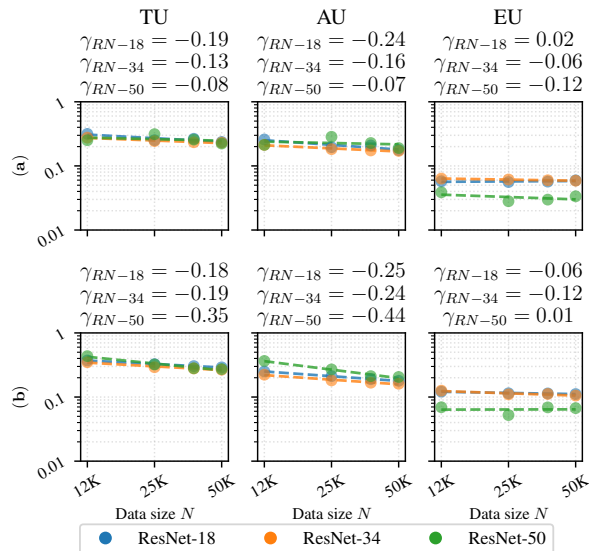


Figure 4. ResNets uncertainties out-of-distribution: We use MCD with $p = 0.2$ in (a) and $p = 0.5$ in (b). For models trained on incrementally larger training subsets of CIFAR-10, we report the predictive uncertainties when testing on the (whole) CIFAR10-C dataset, averaged over all corruption levels (1-5) and corruption types considered. OOD, we expect to observe larger uncertainties - EU, for instance, should decay gradually as the data space becomes increasingly populated with additional samples within the same domain (in-fill).

conduct a study to highlight how different experimental settings lead to different uncertainty behaviors (Figure 8). It is interesting to observe the effect of annealing the learning rate with a cosine scheduler when training on CIFAR-10, suggesting that early-phase uncertainty dynamics in transformers can be sensitive to optimization strategies. Results on ImageNet 32 are reported in Figure 13.

ViT uncertainty scaling with model parameters In ViT models, EU decreases with model size (negative γ across all patch sizes and depths), as it can be observed in Figure 9. We believe that larger ViTs produce smoother representations and show stronger inductive bias toward stable features;

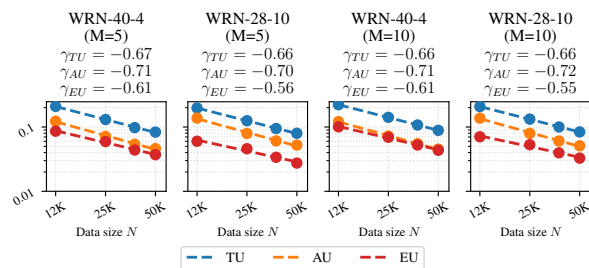


Figure 5. WideResNet -w-d uncertainty scaling on CIFAR-10 dataset: We consider WideResNet-40-4 and WideResNet-28-10 and perform UQ using DE with $M = 5$ and $M = 10$ ensemble members.

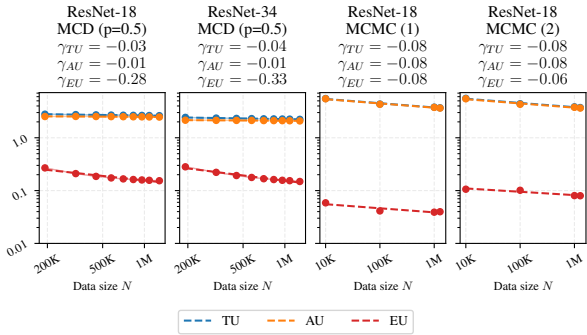


Figure 6. Uncertainty estimates of ResNets on ImageNet-32 dataset: The first two subplots report MCD ($p = 0.5$) uncertainties for ResNet-18 and ResNet-34, trained with fixed learning rate 10^{-3} on 9 increasing subsets of the training data. We also report uncertainties obtained through MCMC considering only the first layer stochastic (MCMC (1)) and only the first two layers stochastic (MCMC (2)) for ResNet-18 trained on 4 increasing subsets of the training data.

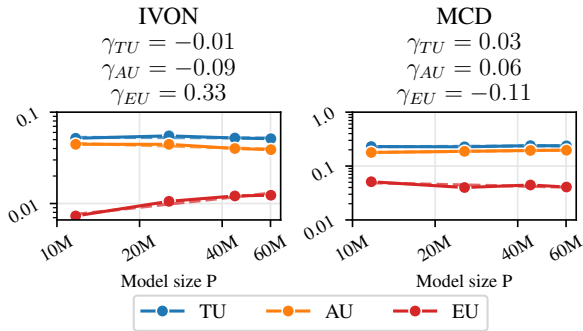


Figure 7. Uncertainty scaling with model parameters of ResNets on CIFAR-10: We evaluate a wide spectrum of ResNet architectures on CIFAR-10 dataset. The corresponding parameter counts are: ResNet-18 (11.7M), ResNet-50 (25.6M), ResNet-101 (44.5M), and ResNet-152 (60.2M). *Left:* We train each model on the entire dataset using the IVON optimizer for 200 epochs, following the setup of Shen et al. (2024) (details in Section D). *Right:* We compare against MCD ($p = 0.5$), training for 400 epochs with SGD and fixed learning rate 10^{-3} .

consequently, different dropout samples yield increasingly similar predictive distributions. In this setting, model size reduces ensemble diversity, and therefore EU contracts.

4.2. Text classification

We firstly investigate the language modality by assessing uncertainty estimates on the pre-trained Phi-2 model (Abdin et al., 2024), applying a Laplace approximation to the posterior over the LoRA parameters (Yang et al., 2024). We fine-tuned the model on qqp and ARC datasets observing that the uncertainties remain flat for every data subset used for fine tuning (see Figure 18). This saturation effect is likely due to the massive amount of data used for pre-training, limiting the expressiveness of the model uncertainty on comparatively much smaller data for fine-tuning.

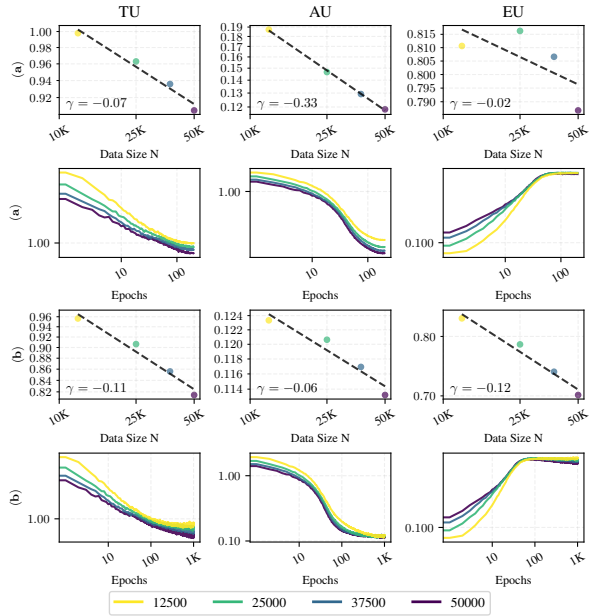


Figure 8. ViT-small uncertainty training dynamics on CIFAR-10 dataset: In (a) we use MCD (fixed $p = 0.5$ both in the embeddings and in the transformer blocks) and we train the model for 200 epochs with Adam optimizer (Kingma & Ba, 2017) and cosine annealing. In (b) we train the same model for 1000 epochs and fixed learning rate 10^{-4} . The training dynamics show that the the shape/speed of convergence of of TU, AU, EU depends on the optimization trajectories underneath.

4.2.1. GPT-2 ON ALGORITHMIC DATASET

We train a GPT-2 model to solve modular arithmetic problems of the form $(a+b) \bmod m =$, where m is the modulus, a and b are integers from 0 to m , and the model learns to predict the token after the $=$ sign. This setup and dataset differ significantly from the vision tasks considered so far, thus providing a complementary testbed for our hypotheses. We experiment using MCD with a dropout rate of $p = 0.1$. In Figure 10 we show predictive uncertainties when training the model on increasing percentages (from 5% to 90%) of the $m = 97$ algorithmic dataset. Similarly to previous experiments, we observe clear scaling laws for all uncertainty metrics considered. Interestingly, more evident uncertainty scaling patterns only emerge after extensive training, suggesting potential links between grokking (Belkin et al., 2019) and uncertainty behavior. The slight uncertainty increase in the last N subset of Figure 10 likely stems from convergence dynamics and limitations of MCD.

4.3. Extrapolation on a toy dataset

We conduct an experiment using a simple MLP on the `two_moons`¹ toy classification dataset to demonstrate the practical application of uncertainty scaling laws. As illus-

¹Dataset available through Scikit-learn (Pedregosa et al., 2011)

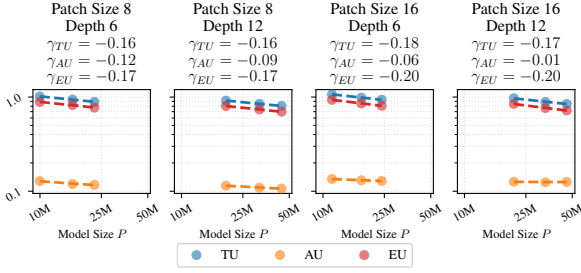


Figure 9. ViT uncertainty scaling with model parameters: We train different sizes of ViT by varying the patch size (8, 16), the number of layers (6, 12) and the number of attention heads (each point corresponds to 8, 16 and 24 attention heads respectively). We use MCD (with fixed $p = 0.5$ both in the embeddings and in the transformer blocks). AU shows minimal dependence on P . TU mirrors the trend of the epistemic component. Overall, the slopes are small in magnitude ($|\gamma| < 0.2$), indicating that uncertainty decreases only slowly with model size.

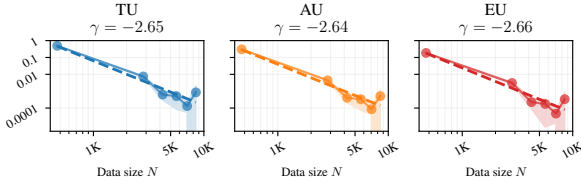


Figure 10. Algorithmic dataset: GPT-2 model on the Algorithmic dataset to learn the modulo addition operation. Results are obtained by training for 10 000 epochs and averaging over 3 seeds.

trated in Figure 11, the EU exhibits a clear power-law decay across the observed range of N . As expected, the AU contribution settles down and plateaus for large values of N , representing the irreducible noise inherent in the task. The TU curve eventually diverges from the power-law trend as it approaches this aleatoric floor. Beyond the extrapolation boundary, the predicted EU remains highly consistent with the actual observed scaling. This is particularly powerful because it demonstrates that training on a relatively small regime, up to just a few thousand data points, allows us to accurately predict the uncertainty behavior we can expect when scaling the data to the order of millions of samples.

5. Theoretical connections

The theory of identifiable models has extensively analyzed asymptotic behaviors, such as posterior contraction and convergence of test loss and generalization error. In this section, we recall how predictive uncertainty contracts with increasing data in Bayesian linear regression, highlight its connection to Watanabe’s Generalization Error, and outline links to SLT.

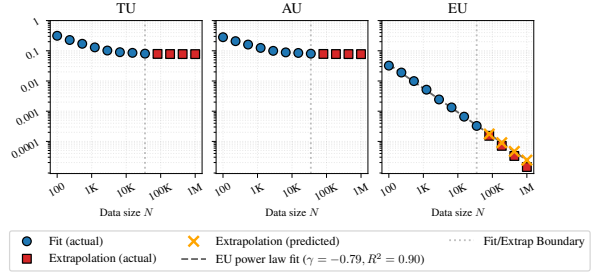


Figure 11. Uncertainty scaling of an MLP on the two_moons dataset: We use Bayesian logistic regression with normal priors on an MLP with two hidden layers of size 32 and tanh activation functions. Posterior inference is performed with HMC sampling (200 posterior samples after 1,000 warm-up steps). Training is carried out on 12 log-spaced values ranging from 100 to 1M and 4 random seeds. Uncertainties are computed on the held-out 5,000 test set.

5.1. Total Uncertainty scaling in Identifiable Parametric Models

We consider Bayesian linear regression $y = \theta^\top \phi(\mathbf{x}) + \epsilon$, where $\theta \in \mathbb{R}^P$ are parameters of interest, and $\phi(\mathbf{x}) = [\phi_1(\mathbf{x}), \phi_2(\mathbf{x}), \dots, \phi_P(\mathbf{x})]^\top$ are basis functions, and assume zero-mean noise $\epsilon \sim \mathcal{N}(0, \sigma^2)$. We define the likelihood over N iid observations $\{\mathbf{X}, \mathbf{y}\} = \{(\mathbf{x}_i, y_i)\}_{i=1}^N$,

$$p(\mathbf{y}|\mathbf{X}, \theta, \sigma^2) = \prod_{n=1}^N \mathcal{N}(y_n | \phi(\mathbf{x}_n)^\top \theta, \sigma^2). \quad (7)$$

By assuming a conjugate Gaussian prior $p(\theta) = \mathcal{N}(\theta | \mathbf{m}_0, \mathbf{S}_0)$ the posterior is also Gaussian with mean $\mathbf{m}_N = \mathbf{S}_N (\mathbf{S}_0^{-1} \mathbf{m}_0 + \sigma^{-2} \Phi^\top \mathbf{y})$ and covariance $\mathbf{S}_N = (\sigma^{-2} \Phi^\top \Phi + \mathbf{S}_0^{-1})^{-1}$.

The predictive posterior for a new test points (\mathbf{x}_*, y_*) is also Gaussian, $p(y_* | \mathbf{x}_*, \mathbf{y}, \mathbf{X}) = \mathcal{N}(y_* | \mathbf{m}_N^\top \phi(\mathbf{x}_*), \sigma_N^2(\mathbf{x}_*))$ with $\sigma_N^2(\mathbf{x}_*) = \sigma^2 + \phi(\mathbf{x}_*)^\top \mathbf{S}_N \phi(\mathbf{x}_*)$.

The predictive variance $\text{Var}[y_* | \mathbf{x}_*, \mathbf{y}, \mathbf{X}]$ decomposes into the uncertainty of data σ^2 (AU), and the uncertainty of parameters $\phi(\mathbf{x}_*)^\top \mathbf{S}_N \phi(\mathbf{x}_*)$ (EU). It can be shown that $\sigma_{N+1}^2(\mathbf{x}_*) \leq \sigma_N^2(\mathbf{x}_*)$ – the posterior distribution becomes narrower as additional data points are observed (Qazaz et al., 1997). Moreover, in the limit of $N \rightarrow \infty$ we get $\sigma_N^2(\mathbf{x}) \rightarrow \sigma^2$: the predictive uncertainty converges to its irreducible AU component.

5.2. Singular Learning Theory

Our speculative theoretical link is SLT, which provides insights into the learning dynamics of highly overparameterized models. The Fisher information of deep neural networks is often singular at certain parameter values; despite

forming a measure-zero subset, these singularities significantly influence learning. SLT proves that the asymptotic properties of learning are shaped by the geometry near such degenerate points (Watanabe, 2009; 2018). Here we limit ourselves to connect this to the TU in Bayesian linear regression. Using Watanabe’s notation:

$$F_N = -\log p(\mathbf{y}_N | \mathbf{X}_N) = -\log \int p(\mathbf{y}_N | \mathbf{X}_N, \boldsymbol{\theta}) p(\boldsymbol{\theta}) d\boldsymbol{\theta} \quad (8)$$

is the Negative Marginal Log Likelihood (NMLL) of the data \mathbf{X}_N of size N . By denoting the true conditional distribution $p(y) \equiv p(y_{N+1} | \mathbf{x}_{N+1}, \boldsymbol{\theta}_{\text{true}})$ (e.g., $y_{N+1} \sim \mathcal{N}(\boldsymbol{\theta}_{\text{true}}^\top \mathbf{x}_{N+1}, \sigma_{\text{true}}^2)$), the generalization error $G_N = \mathbb{E}_{p(y)}[F_{N+1}] - F_N$ measures the expected increase in marginal likelihood when training with one additional data point (see Section A.2). This can be rewritten as:

$$G_N = -\mathbb{E}_{p(y)} \left[\underbrace{\log p(y_{N+1} | \mathbf{x}_{N+1}, \mathbf{X}_N, \mathbf{y}_N)}_{q_N(y)} \right], \quad (9)$$

which reduces to the log posterior predictive distribution for the $(N+1)$ ’th datapoint given the first N datapoints, under the true conditional distribution $p(y)$. By denoting the posterior predictive $q_N(y)$, we can manipulate the expression in Equation (9) to obtain:

$$G_N = \underbrace{\frac{1}{2} \log(2\pi e \sigma_{\text{true}}^2)}_{\text{aleatoric uncertainty}} + \underbrace{\text{KL}[p(y) || q_N(y)]}_{\text{epistemic uncertainty}}, \quad (10)$$

where $\text{KL}[p(y) || q_N(y)]$ is the KL divergence between the true and the posterior predictive distribution, quantifying the EU arising from limited knowledge of the model parameters. By looking at the asymptotic expression of TU as $N \rightarrow \infty$ and by taking, without loss of generality, identity basis functions, we get:

$$\begin{aligned} \text{TU}(\mathbf{x}_{N+1}) &= \mathbb{H}[q_N(y)] \\ &= \frac{1}{2} \log(2\pi e \sigma_{\text{true}}^2) + \frac{\mathbf{x}_{N+1}^\top \boldsymbol{\Sigma}_{\mathbf{X}_{N+1}}^{-1} \mathbf{x}_{N+1}}{2(N+1)} \\ &\quad + O\left(\frac{1}{(N+1)^2}\right). \end{aligned} \quad (11)$$

As more data is collected, the predictive posterior $q_N(y)$ converges to the true predictive distribution $p(y)$. Consequently, the generalization error G_N asymptotically approaches the irreducible AU. Similarly, the TU converges to the aleatoric component as the epistemic part vanishes. In Watanabe (1999) it’s proved an asymptotic expansion of G_N which is proportional to the effective dimensionality of the model (Section A.2.1).

Recent advances on the effective dimensionality of deep models (Lau et al., 2024; Chen et al., 2024) appear especially promising, and we intend to investigate such formal connections in future work. We further hypothesize that concepts from Statistical Physics may help explain the scaling behaviors we observed.

6. Conclusions

Inspired by recent work on scaling laws in deep learning, we investigated whether similar patterns hold for predictive uncertainties. Across vision and language tasks, we find scaling behaviors robust to architecture, posterior approximation, and hyper-parameters. Building on SLT, we provide theoretical insights connecting generalization error and predictive uncertainty, showing why information-theoretic measures scale with dataset size. However, deriving exact power-law coefficients is difficult, as they vary unpredictably with design choices. Our results suggest practical strategies for extrapolating uncertainties to large N , such as estimating how much data is needed for ensemble predictions to converge. They also point to applications in active learning, where one can predict the marginal uncertainty reduction from additional data to guide annotation budgets. More broadly, while scaling laws are predictive, they are not universal but depend on how the loss landscape is traversed, underscoring the need to tailor optimization strategies to each task.

Limitations and future work A key limitation is that we do not yet have a formal theory that predicts the empirical scaling exponents γ of deep networks from SLT invariants or other geometric quantities. Moreover, optimization effects remain only partially characterized: we observe that simple optimization settings (e.g., fixed learning rates) can yield clearer scaling than more complex schedules in some settings, but we do not yet explain when and why this occurs. Finally, in transfer and fine-tuning settings, large-scale pre-training can saturate uncertainty estimates, potentially masking scaling behavior on smaller downstream datasets.

Future work will aim to (i) connect deep-network scaling exponents to effective model complexity (e.g., effective dimensionality or RLCT-like quantities), (ii) study more in depth the scaling with compute budget and model size, and (iii) relate uncertainty scaling to theoretical limits such as wide-network GP approximations.

Impact Statement

By characterizing uncertainty scaling in modern neural networks, this work provides essential insights for ensuring the reliability and safety of large-scale AI systems.

References

- Bayesian generalization error in linear neural networks with concept bottleneck structure and multitask formulation. *Neurocomputing*, 638:130165, 2025.
- Abdin et al., M. I. Phi-3 technical report: A highly capable language model locally on your phone. Technical Report MSR-TR-2024-12, Microsoft, August 2024.
- Ansuini, A., Laio, A., Macke, J., and Zoccolan, D. Intrinsic dimension of data representations in deep neural networks. In *Advances in Neural Information Processing Systems*, 2019.
- Antoran, J., Janz, D., Allingham, J. U., Daxberger, E., Barbano, R. R., Nalisnick, E., and Hernandez-Lobato, J. M. Adapting the linearised Laplace model evidence for modern deep learning. In *International Conference on Machine Learning*, 2022.
- Bahri, Y., Dyer, E., Kaplan, J., Lee, J., and Sharma, U. Explaining neural scaling laws. *Proceedings of the National Academy of Sciences*, 121(27), 2024.
- Belkin, M., Hsu, D., Ma, S., and Mandal, S. Reconciling modern machine-learning practice and the classical bias–variance trade-off. *Proceedings of the National Academy of Sciences*, 2019.
- Cam, L. *On Some Asymptotic Properties of Maximum Likelihood Estimates and Related Bayes’ Estimates*. University of California Press, 1953.
- Chen, D., Chang, W.-K., and Chaudhari, P. Learning capacity: A measure of the effective dimensionality of a model. *arXiv*, 2024.
- Chen, T., Fox, E., and Guestrin, C. Stochastic gradient Hamiltonian Monte Carlo. In *International Conference on Machine Learning*, 2014.
- de Jong, I. P., Sburlea, A. I., Sabatelli, M., and Valdenegro-Toro, M. Measuring uncertainty disentanglement error in classification, 2025.
- Dosovitskiy, A., Beyer, L., Kolesnikov, A., Weissenborn, D., Zhai, X., Unterthiner, T., Dehghani, M., Minderer, M., Heigold, G., Gelly, S., Uszkoreit, J., and Houlsby, N. An image is worth 16x16 words: Transformers for image recognition at scale. In *International Conference on Learning Representations*, 2021.
- Fellaji, M. and Pennerath, F. The epistemic uncertainty hole: An issue of Bayesian neural networks. *arXiv*, 2024.
- Foret, P., Kleiner, A., Mobahi, H., and Neyshabur, B. Sharpness-aware minimization for efficiently improving generalization. *arXiv*, 2020.
- Gal, Y. and Ghahramani, Z. Dropout as a Bayesian approximation: Representing model uncertainty in deep learning. In *International Conference on Machine Learning*, 2016.
- Gal, Y., Hron, J., and Kendall, A. Concrete dropout. In *Advances in Neural Information Processing Systems*, 2017.
- Gelberg, Y., van der Ouderaa, T. F. A., van der Wilk, M., and Gal, Y. Variational inference failures under model symmetries: Permutation invariant posteriors for Bayesian neural networks. In Vadgama, S., Bekkers, E., Pouplin, A., Kaba, S.-O., Walters, R., Lawrence, H., Emerson, T., Kvinge, H., Tomczak, J., and Jegelka, S. (eds.), *Proceedings of the Geometry-grounded Representation Learning and Generative Modeling Workshop (GRaM)*, volume 251 of *Proceedings of Machine Learning Research*, pp. 233–248. PMLR, 29 Jul 2024.
- Graves, A. Practical variational inference for neural networks. In *Advances in Neural Information Processing Systems*, 2011.
- He, K., Zhang, X., Ren, S., and Sun, J. Deep residual learning for image recognition. *IEEE Conference on Computer Vision and Pattern Recognition*, 2016.
- Henighan, T., Kaplan, J., Katz, M., Chen, M., Hesse, C., Jackson, J., Jun, H., Brown, T. B., Dhariwal, P., Gray, S., Hallacy, C., Mann, B., Radford, A., Ramesh, A., Ryder, N., Ziegler, D. M., Schulman, J., Amodei, D., and McCandlish, S. Scaling laws for autoregressive generative modeling. *arXiv*, 2020.
- Hestness, J., Narang, S., Ardalani, N., Damos, G. F., Jun, H., Kianinejad, H., Patwary, M. A., Yang, Y., and Zhou, Y. Deep learning scaling is predictable, empirically. *ArXiv*, 2017.
- Hoffmann, J., Borgeaud, S., Mensch, A., Buchatskaya, E., Cai, T., Rutherford, E., de Las Casas, D., Hendricks, L. A., Welbl, J., Clark, A., Hennigan, T., Noland, E., Millican, K., van den Driessche, G., Damoc, B., Guy, A., Osindero, S., Simonyan, K., Elsen, E., Vinyals, O., Rae, J. W., and Sifre, L. Training compute-optimal large language models. In *NeurIPS*, 2022.
- Hüllermeier, E. and Waegeman, W. Aleatoric and epistemic uncertainty in machine learning: an introduction to concepts and methods. *Machine Learning*, 2021.
- Immer, A., Korzepa, M., and Bauer, M. Improving predictions of bayesian neural nets via local linearization. In *International conference on artificial intelligence and statistics*, pp. 703–711. PMLR, 2021.
- Izmailov, P., Vikram, S., Hoffman, M. D., and Wilson, A. G. G. What are Bayesian neural network posteriors really like? In *International conference on machine learning*, pp. 4629–4640. PMLR, 2021.

- Kaplan, J., McCandlish, S., Henighan, T., Brown, T. B., Chess, B., Child, R., Gray, S., Radford, A., Wu, J., and Amodei, D. Scaling laws for neural language models. *ArXiv*, 2020.
- Khan, M. E. and Rue, H. The Bayesian learning rule. *Journal of Machine Learning Research*, 24(281):1–46, 2023.
- Kim, B. J., Choi, H., Jang, H., Lee, D., and Kim, S. W. How to use dropout correctly on residual networks with batch normalization. In *Conference on Uncertainty in Artificial Intelligence*, 2023.
- Kingma, D. P. and Ba, J. Adam: A method for stochastic optimization, 2017.
- Kirsch, A. (implicit) ensembles of ensembles: Epistemic uncertainty collapse in large models. In *NeurIPS 2024 Workshop on Bayesian Decision-making and Uncertainty*, 2024.
- Lakshminarayanan, B., Pritzel, A., and Blundell, C. Simple and scalable predictive uncertainty estimation using deep ensembles. In *Advances in Neural Information Processing Systems*, 2017.
- Lau, E., Furman, Z., Wang, G., Mufet, D., and Wei, S. The local learning coefficient: A singularity-aware complexity measure. *arXiv*, 2024.
- Laurent, O., Aldea, E., and Franchi, G. A symmetry-aware exploration of Bayesian neural network posteriors, 2023.
- Loshchilov, I. and Hutter, F. Decoupled weight decay regularization, 2019.
- Lu, H., Liu, X., Zhou, Y., Li, Q., Keutzer, K., Mahoney, M. W., Yan, Y., Yang, H., and Yang, Y. Sharpness-diversity tradeoff: improving flat ensembles with sharp-balance. *Advances in Neural Information Processing Systems*, 37:136727–136762, 2024.
- MacKay, D. J. Bayesian neural networks and density networks. *Nuclear Instruments and Methods in Physics Research Section A*, 354(1):73–80, 1995.
- Mucsányi, B., Kirchhof, M., and Oh, S. J. Benchmarking uncertainty disentanglement: Specialized uncertainties for specialized tasks. In Globerson, A., Mackey, L., Belgrave, D., Fan, A., Paquet, U., Tomczak, J., and Zhang, C. (eds.), *Advances in Neural Information Processing Systems*, volume 37, pp. 50972–51038. Curran Associates, Inc., 2024.
- Nanda, N., Chan, L., Lieberum, T., Smith, J., and Steinhart, J. Progress measures for grokking via mechanistic interpretability. *arXiv*, 2023.
- Neal, R. *Bayesian Learning for Neural Networks*. Springer-Verlag, 1996.
- Papamarkou, T., Skoularidou, M., Palla, K., Aitchison, L., Arbel, J., Dunson, D., Filippone, M., Fortuin, V., Hennig, P., Hernández-Lobato, J. M., Hubin, A., Immer, A., Karaletsos, T., Khan, M. E., Kristiadi, A., Li, Y., Mandt, S., Nemeth, C., Osborne, M. A., Rudner, T. G. J., Rügamer, D., Teh, Y. W., Welling, M., Wilson, A. G., and Zhang, R. Position: Bayesian deep learning is needed in the age of large-scale AI. In *International Conference on Machine Learning*, 2024.
- Pedregosa, F., Varoquaux, G., Gramfort, A., Michel, V., Thirion, B., Grisel, O., Blondel, M., Prettenhofer, P., Weiss, R., Dubourg, V., Vanderplas, J., Passos, A., Cournapeau, D., Brucher, M., Perrot, M., and Duchesnay, E. Scikit-learn: Machine learning in Python. *Journal of Machine Learning Research*, 12:2825–2830, 2011.
- Qazaz, C. S., Williams, C. K. I., and Bishop, C. M. An upper bound on the Bayesian error bars for generalized linear regression. In *Proceedings of the First International Conference on Mathematics of Neural Networks*, 1997.
- Ritter, H., Botev, A., and Barber, D. A scalable Laplace approximation for neural networks. In *International conference on learning representations*, 2018.
- Rossi, S., Singh, A., and Hannagan, T. On permutation symmetries in Bayesian neural network posteriors: a variational perspective. In Oh, A., Naumann, T., Globerson, A., Saenko, K., Hardt, M., and Levine, S. (eds.), *Advances in Neural Information Processing Systems*, volume 36, pp. 69032–69053. Curran Associates, Inc., 2023.
- Sharma, M., Farquhar, S., Nalisnick, E., and Rainforth, T. Do Bayesian neural networks need to be fully stochastic? In *International Conference on Artificial Intelligence and Statistics*, 2023.
- Sharma, U. and Kaplan, J. Scaling laws from the data manifold dimension. *Journal of Machine Learning Research*, 23(9):1–34, 2022.
- Shen, Y., Daheim, N., Cong, B., Nickl, P., Marconi, G. M., Raoul, B. C. E. M., Yokota, R., Gurevych, I., Cremers, D., Khan, M. E., and Möllenhoff, T. Variational learning is effective for large deep networks. In Salakhutdinov, R., Kolter, Z., Heller, K., Weller, A., Oliver, N., Scarlett, J., and Berkenkamp, F. (eds.), *Proceedings of the 41st International Conference on Machine Learning*, volume 235 of *Proceedings of Machine Learning Research*, pp. 44665–44686. PMLR, 21–27 Jul 2024.
- Tran, B.-H., Rossi, S., Milios, D., and Filippone, M. All you need is a good functional prior for Bayesian deep learning. *Journal of Machine Learning Research*, 2022.

- Watanabe, S. Algebraic analysis for non-regular learning machines. In *Advances in Neural Information Processing Systems*, 1999.
- Watanabe, S. *Algebraic Geometry and Statistical Learning Theory*. Cambridge University Press, 2009.
- Watanabe, S. *Mathematical Theory of Bayesian Statistics*. CRC Press, Taylor & Francis Group, 2018.
- Welling, M. and Teh, Y. W. Bayesian learning via stochastic gradient Langevin dynamics. In *International Conference on International Conference on Machine Learning*, 2011.
- Wimmer, L., Sale, Y., Hofman, P., Bischl, B., and Hüllermeier, E. Quantifying aleatoric and epistemic uncertainty in machine learning: Are conditional entropy and mutual information appropriate measures? In *Conference on Uncertainty in Artificial Intelligence*, 2023.
- Yang, A., Robeyns, M., Wang, X., and Aitchison, L. Bayesian low-rank adaptation for large language models. 2024.
- Zagoruyko, S. and Komodakis, N. Wide residual networks. *arXiv*, 2016.

A. Connections with SLT

Our theoretical framework is motivated by SLT, which offers geometric insights into the learning dynamics of highly overparameterized models. In deep neural networks, the Fisher information matrix is frequently singular; although these singularities form a measure-zero subset of the parameter space, they profoundly influence the learning process. SLT demonstrates that the asymptotic properties of learning are governed by the algebraic geometry near these degenerate points (Watanabe, 2009; 2018).

In this section, we restrict our analysis to the connection between SLT and TU within the context of Bayesian linear regression. Following the notation of Watanabe (2009), we define the NMLL (or free energy) of a dataset \mathbf{X}_N of size N as:

$$F_N = -\log p(\mathbf{y}_N | \mathbf{X}_N) = -\log \int p(\mathbf{y}_N | \mathbf{X}_N, \boldsymbol{\theta}) p(\boldsymbol{\theta}) d\boldsymbol{\theta}. \quad (12)$$

The generalization error, G_N , measures the expected negative log-likelihood of an unseen data point $(\mathbf{x}_{N+1}, y_{N+1})$ sampled from the true distribution. It is defined as:

$$G_N = \mathbb{E}_{p(y_{N+1} | \mathbf{x}_{N+1}, \boldsymbol{\theta}_{\text{true}})} [-\log p(y_{N+1} | \mathbf{x}_{N+1}, \mathbf{X}_N, \mathbf{y}_N)] \quad (13)$$

$$= -\mathbb{E}_{p(y)} [\log q_N(y)], \quad (14)$$

where $p(y)$ denotes the true process $y_{N+1} \sim \mathcal{N}(y_{N+1} | \boldsymbol{\theta}_{\text{true}}^\top \mathbf{x}_{N+1}, \sigma_{\text{true}}^2)$ and $q_N(y)$ represents the posterior predictive distribution given the first N data points.

We can decompose the generalization error in Equation (13) into aleatoric and epistemic components:

$$\begin{aligned} G_N &= \mathbb{E}_{p(y)} [-\log q_N(y)] \\ &= \mathbb{E}_{p(y)} [-\log p(y) + \log p(y) - \log q_N(y)] \\ &= \underbrace{\mathbb{H}[p(y)]}_{\text{aleatoric uncertainty}} + \underbrace{\text{KL}[p(y) || q_N(y)]}_{\text{epistemic uncertainty}}. \end{aligned} \quad (15)$$

Here, $\mathbb{H}[p(y)] = \frac{1}{2} \log(2\pi e \sigma_{\text{true}}^2)$ represents the irreducible noise (entropy) of the true process, while the KL divergence quantifies the EU arising from the deviation of the posterior predictive from the truth.

Examining the asymptotic behavior of TU as $N \rightarrow \infty$, and assuming identity basis functions without loss of generality, we obtain:

$$\text{TU}(\mathbf{x}_{N+1}) = \mathbb{H}[q_N(y)] = \frac{1}{2} \log(2\pi e \sigma_{\text{true}}^2) + \frac{\mathbf{x}_{N+1}^\top \boldsymbol{\Sigma}_{\mathbf{X}_{N+1}}^{-1} \mathbf{x}_{N+1}}{2(N+1)} + O\left(\frac{1}{N^2}\right). \quad (16)$$

As $N \rightarrow \infty$, the posterior predictive $q_N(y)$ converges to the true distribution $p(y)$. Consequently, the epistemic term vanishes, and both G_N and TU asymptotically approach the irreducible aleatoric entropy. Watanabe (1999) derives a rigorous asymptotic expansion of G_N , showing it is proportional to the effective dimensionality of the model (see Section A.2.1).

Recent advances in estimating the effective dimensionality of deep models (Lau et al., 2024; Chen et al., 2024) appear especially promising. We intend to investigate these formal connections in future work, hypothesizing that concepts from Statistical Physics may further elucidate the observed scaling behaviors.

A.1. Total Uncertainty in Bayesian Linear Regression

We consider a class of models defined as a linear combination of fixed nonlinear functions of the input variables of the form:

$$y(\mathbf{x}, \boldsymbol{\theta}) = \sum_{j=0}^{M-1} \theta_j \phi_j(\mathbf{x}) = \boldsymbol{\theta}^\top \boldsymbol{\phi}(\mathbf{x}), \quad (17)$$

where $\boldsymbol{\theta} = (\theta_0, \dots, \theta_{M-1})^\top$ are model parameters and $\boldsymbol{\phi} = (\phi_0, \dots, \phi_{M-1})^\top$ are known as *basis functions* which allow $y(\mathbf{x}, \boldsymbol{\theta})$ to be a non-linear function of the input \mathbf{x} .

We consider the target variable y that is given by a deterministic function $y(\mathbf{x}, \boldsymbol{\theta})$ plus additive Gaussian noise:

$$y = \boldsymbol{\theta}^\top \boldsymbol{\phi}(\mathbf{x}) + \epsilon, \quad (18)$$

where $\boldsymbol{\theta}$ is treated as a random vector and $\epsilon \sim \mathcal{N}(0, \sigma^2)$, obtaining

$$p(y|\mathbf{x}, \boldsymbol{\theta}, \sigma^2) = \mathcal{N}(y|\boldsymbol{\phi}(\mathbf{x})^\top \boldsymbol{\theta}, \sigma^2). \quad (19)$$

We consider a supervised learning problem with N input-label training pairs $\{\mathbf{X}, \mathbf{y}\} = \{(\mathbf{x}_i, y_i)\}_{i=1}^N$. Assuming that the data points are drawn independently from Equation (19), the likelihood becomes:

$$p(\mathbf{y}|\mathbf{X}, \boldsymbol{\theta}, \sigma^2) = \prod_{n=1}^N \mathcal{N}(y_n|\boldsymbol{\phi}(\mathbf{x}_n)^\top \boldsymbol{\theta}, \sigma^2). \quad (20)$$

According to the transformation of the features introduced by the set of basis functions $\boldsymbol{\phi}$, we define the design matrix $\boldsymbol{\Phi} \in \mathbb{R}^{N \times M}$ with entries $\boldsymbol{\Phi}_{nj} = \phi_j(\mathbf{x}_n)$. We assume a conjugate prior over $\boldsymbol{\theta}$:

$$p(\boldsymbol{\theta}) = \mathcal{N}(\boldsymbol{\theta}|\boldsymbol{\mu}_0, \boldsymbol{\Sigma}_0). \quad (21)$$

From Bayes' theorem, the posterior can be derived in closed form leading to the following result:

$$p(\boldsymbol{\theta}|\mathbf{y}, \mathbf{X}) = \mathcal{N}(\boldsymbol{\theta}|\boldsymbol{\mu}_N, \boldsymbol{\Sigma}_N), \quad (22)$$

$$\boldsymbol{\mu}_N = \boldsymbol{\Sigma}_N \left(\boldsymbol{\Sigma}_0^{-1} \boldsymbol{\mu}_0 + \sigma^{-2} \boldsymbol{\Phi}^\top \mathbf{y} \right), \quad (23)$$

$$\boldsymbol{\Sigma}_N = \left(\sigma^{-2} \boldsymbol{\Phi}^\top \boldsymbol{\Phi} + \boldsymbol{\Sigma}_0^{-1} \right)^{-1}. \quad (24)$$

We are interested in the predictive uncertainty for a new test point (\mathbf{x}_*, y_*) so we inspect the predictive posterior and its properties:

$$\begin{aligned} p(y_*|\mathbf{x}_*, \mathbf{y}, \mathbf{X}) &= \int p(y_*|\mathbf{x}_*, \boldsymbol{\theta}) p(\boldsymbol{\theta}|\mathbf{y}, \mathbf{X}) d\boldsymbol{\theta} \\ &= \mathcal{N}(y_*|\boldsymbol{\mu}_N^\top \boldsymbol{\phi}(\mathbf{x}_*), \underbrace{\sigma^2 + \boldsymbol{\phi}(\mathbf{x}_*)^\top \boldsymbol{\Sigma}_N \boldsymbol{\phi}(\mathbf{x}_*)}_{\mathbb{V}[y_*|\mathbf{x}_*, \mathbf{y}]}) \end{aligned} \quad (25)$$

where $\boldsymbol{\mu}_N$ and $\boldsymbol{\Sigma}_N$ are the posterior mean and covariance matrix. From the predictive variance $\mathbb{V}[y_*|\mathbf{x}_*, \mathbf{y}]$ we identify two components: (i) σ^2 which represents the uncertainty related to the data noise (AU) and (ii) $\boldsymbol{\phi}(\mathbf{x}_*)^\top \boldsymbol{\Sigma}_N \boldsymbol{\phi}(\mathbf{x}_*)$ which is the uncertainty associated with model parameters (EU). As we discuss in Section 5.1, by defining $\mathbb{V}[y_*|\mathbf{x}_*, \mathbf{y}] := \sigma_N^2(\mathbf{x})$ as the predictive uncertainty for a new test point \mathbf{x} when training on N input points, we have that $\sigma_{N+1}^2(\mathbf{x}) \leq \sigma_N^2(\mathbf{x})$, meaning that the posterior distribution becomes narrower as additional data points are observed (Qazaz et al., 1997). Moreover, $\lim_{N \rightarrow \infty} \sigma_N^2(\mathbf{x}) = \sigma^2$; that is, in the infinite data regime, the predictive uncertainty converges to its irreducible component, AU.

A.1.1. FROM POSTERIOR PREDICTIVE VARIANCE TO TOTAL UNCERTAINTY

We now derive an expression for the (total) predictive uncertainty associated with a new data point (\mathbf{x}, y) , defined as the entropy of the predictive posterior:

$$\begin{aligned}
 \text{TU}(\mathbf{x}) &= \mathbb{H}[p(y|\mathbf{x}, \mathbf{y}, \mathbf{X})] \\
 &= \frac{1}{2} \log(2\pi e \sigma_N^2(\mathbf{x})) \\
 &= \frac{1}{2} \log\left(2\pi e \left(\sigma^2 + \phi(\mathbf{x})^\top \left(\sigma^{-2} \Phi^\top \Phi + \Sigma_0^{-1}\right)^{-1} \phi(\mathbf{x})\right)\right) \\
 &= \frac{1}{2} \log\left(2\pi e \sigma^2 \left(1 + \sigma^{-2} \phi(\mathbf{x})^\top \left(\sigma^{-2} \Phi^\top \Phi + \Sigma_0^{-1}\right)^{-1} \phi(\mathbf{x})\right)\right) \\
 &= \frac{1}{2} \log(2\pi e \sigma^2) + \frac{1}{2} \log\left(1 + \sigma^{-2} \phi(\mathbf{x})^\top \left(\sigma^{-2} \Phi^\top \Phi + \Sigma_0^{-1}\right)^{-1} \phi(\mathbf{x})\right) \\
 &= \underbrace{\frac{1}{2} \log(2\pi e \sigma^2)}_{\text{AU}(\mathbf{x})} + \underbrace{\frac{1}{2N} \phi(\mathbf{x})^\top \Sigma_\phi^{-1} \phi(\mathbf{x})}_{\text{EU}(\mathbf{x})} + O\left(\frac{1}{N^2}\right)
 \end{aligned} \tag{26}$$

In the previous derivation, we assume $\mathbf{X} = (\mathbf{x}_1, \dots, \mathbf{x}_N)$ to be a collection of IID samples with $\mathbf{0}$ mean and Σ_x covariance matrix. The same holds for Φ where samples $\phi(\mathbf{x})$ are drawn independently from a distribution with $\mathbf{0}$ mean and Σ_ϕ covariance matrix. By the Law of Large Numbers $\frac{1}{N} \Phi^\top \Phi \rightarrow \mathbb{E}[\phi(\mathbf{x})\phi(\mathbf{x})^\top] = \Sigma_\phi$ as $N \rightarrow \infty$ which implies $\Phi^\top \Phi \rightarrow N \Sigma_\phi$. In addition, for large N the Σ_0^{-1} term vanishes. This shows that as $N \rightarrow \infty$, TU approaches AU and the EU decays with rate $\frac{1}{N}$.

A.2. Total Uncertainty and Generalization Error for linear models

In this Section we formally derive a connection between the Watanabe generalization error G_N and the Total Uncertainty (TU) for Bayesian linear models. Using the notation from [Watanabe \(2009; 2018\)](#) the generalization error G_N and the Free Energy F_N are defined as:

$$G_N = \mathbb{E}_{p(y_{N+1}|\mathbf{x}_{N+1}, \boldsymbol{\theta}_{\text{true}})}[F_{N+1}] - F_N \tag{27}$$

$$F_N = -\log p(\mathbf{y}_N|\mathbf{X}_N) = -\log \int p(\mathbf{y}_N|\mathbf{X}_N, \boldsymbol{\theta}) p(\boldsymbol{\theta}) d\boldsymbol{\theta}. \tag{28}$$

We consider the same linear model of Section [A.1](#) and without loss of generality we set the basis functions to be identity functions, i.e., $\phi(\mathbf{x}) = \mathbf{x}$. We also introduce $\boldsymbol{\theta}_{\text{true}}$, the set of underlying true parameters. A new data point $(\mathbf{x}_{N+1}, y_{N+1})$ is generated according to the true process:

$$y_{N+1} \sim \mathcal{N}(y_{N+1}|\mathbf{x}_{N+1}, \boldsymbol{\theta}_{\text{true}}) = \mathcal{N}(y_{N+1}|\boldsymbol{\theta}_{\text{true}}^\top \mathbf{x}_{N+1}, \sigma_{\text{true}}^2). \tag{29}$$

The free energy F_N is defined as the negative log marginal likelihood:

$$\begin{aligned}
 F_N &= -\log p(\mathbf{y}_N|\mathbf{X}_N) \\
 &= -\log \int p(\mathbf{y}_N|\mathbf{X}_N, \boldsymbol{\theta}) p(\boldsymbol{\theta}) d\boldsymbol{\theta} \\
 &= -\log \int \left(\prod_{n=1}^N p(y_n|\mathbf{x}_n, \boldsymbol{\theta}) \right) p(\boldsymbol{\theta}) d\boldsymbol{\theta}.
 \end{aligned} \tag{30}$$

We now relate F_{N+1} and F_N , the free energy for $N+1$ and N input points, respectively:

$$\begin{aligned}
 F_{N+1} &= -\log p(Y_{N+1}|\mathbf{X}_{N+1}) \\
 &= -\log p(y_{N+1}, \mathbf{y}_N | \mathbf{x}_{N+1}, \mathbf{X}_N) \\
 &= -\log p(y_{N+1} | \mathbf{x}_{N+1}, D_N) p(\mathbf{y}_N | \mathbf{X}_N) \\
 &= -\log p(y_{N+1} | \mathbf{x}_{N+1}, D_N) - \log p(\mathbf{y}_N | \mathbf{X}_N) \\
 &= -\log p(y_{N+1} | \mathbf{x}_{N+1}, D_N) + F_N
 \end{aligned} \tag{31}$$

where $D_N = \{\mathbf{X}_N, \mathbf{y}_N\}$ and $p(y_{N+1} | \mathbf{x}_{N+1}, D_N)$ is the posterior predictive distribution for the $(N+1)$ data point given the first N data points:

$$\begin{aligned}
 p(y_{N+1} | \mathbf{x}_{N+1}, D_N) &= \int p(y_{N+1} | \mathbf{x}_{N+1}, \boldsymbol{\theta}) p(\boldsymbol{\theta} | D_N) d\boldsymbol{\theta} \\
 &= \mathcal{N}(y_{N+1} | \mu_{\text{pred}}, \sigma_{\text{pred}}^2),
 \end{aligned} \tag{32}$$

$$\mu_{\text{pred}} := \mathbb{E}[y_{N+1} | \mathbf{x}_{N+1}, D_N] = \boldsymbol{\mu}_N^\top \mathbf{x}_{N+1} \tag{33}$$

$$\sigma_{\text{pred}}^2 := \mathbb{V}[y_{N+1} | \mathbf{x}_{N+1}, D_N] = \sigma_{\text{true}}^2 + \mathbf{x}_{N+1}^\top \boldsymbol{\Sigma}_N \mathbf{x}_{N+1}. \tag{34}$$

Let's simplify the notation: we rename the new data point y_{N+1} simply y such that $p(y) := p(y_{N+1} | \mu_{\text{true}}, \sigma_{\text{true}}^2)$ where $\mu_{\text{true}} := \boldsymbol{\theta}_{\text{true}}^\top \mathbf{x}_{N+1}$. We can now compute the generalization error:

$$\begin{aligned}
 G_N &= \mathbb{E}_{p(y)}[F_{N+1}] - F_N \\
 &= \mathbb{E}_{p(y)}[F_{N+1} - F_N] \\
 &= \mathbb{E}_{p(y)}[-\log p(y_{N+1} | \mathbf{x}_{N+1}, D_N)] \\
 &= \mathbb{E}_{p(y)} \left[\frac{1}{2} \log(2\pi\sigma_{\text{pred}}^2) + \frac{(y - \mu_{\text{pred}})^2}{2\sigma_{\text{pred}}^2} \right] \\
 &= \frac{1}{2} \log(2\pi\sigma_{\text{pred}}^2) + \frac{\sigma_{\text{true}}^2 + (\mu_{\text{true}} - \mu_{\text{pred}})^2}{2\sigma_{\text{pred}}^2} \\
 &= \underbrace{\mathbb{H}[\mathcal{N}(y | \mu_{\text{true}}, \sigma_{\text{true}}^2)]}_{\text{AU}(\mathbf{x}_{N+1})} + \underbrace{\text{KL}[\mathcal{N}(y | \mu_{\text{true}}, \sigma_{\text{true}}^2) || \mathcal{N}(y | \mu_{\text{pred}}, \sigma_{\text{pred}}^2)]}_{\text{EU}(\mathbf{x}_{N+1})}
 \end{aligned} \tag{35}$$

where we used the fact that $\mathbb{E}_{p(y)}[(y - \mu_{\text{pred}})^2] = \mathbb{V}_{p(y)}[y] + (\mu_{\text{true}} - \mu_{\text{pred}})^2 = \sigma_{\text{true}}^2 + (\mu_{\text{true}} - \mu_{\text{pred}})^2$ and:

$$\mathbb{H}[\mathcal{N}(y | \mu_{\text{true}}, \sigma_{\text{true}}^2)] = \frac{1}{2} \log(2\pi e \sigma_{\text{true}}^2) \tag{36}$$

$$\text{KL}[\mathcal{N}(y | \mu_{\text{true}}, \sigma_{\text{true}}^2) || \mathcal{N}(y | \mu_{\text{pred}}, \sigma_{\text{pred}}^2)] = \frac{1}{2} \log \left(\frac{\sigma_{\text{pred}}^2}{\sigma_{\text{true}}^2} \right) + \frac{\sigma_{\text{true}}^2 + (\mu_{\text{true}} - \mu_{\text{pred}})^2}{2\sigma_{\text{pred}}^2} - \frac{1}{2}. \tag{37}$$

This is closely related to the asymptotic expression we derived for TU in Section A.1.1 where, if we now consider identity basis functions and a test point \mathbf{x}_{N+1} , it becomes:

$$\text{TU}(\mathbf{x}_{N+1}) = \underbrace{\frac{1}{2} \log(2\pi e \sigma_{\text{true}}^2)}_{\text{AU}(\mathbf{x}_{N+1})} + \underbrace{\frac{1}{2(N+1)} \mathbf{x}_{N+1}^\top \boldsymbol{\Sigma}_X^{-1} \mathbf{x}_{N+1}}_{\text{EU}(\mathbf{x}_{N+1})} + O\left(\frac{1}{(N+1)^2}\right) \tag{38}$$

In terms of generalization error G_N , as the posterior predictive $q_N(y)$ moves closer to the true data generating distribution $p(y)$, the KL term goes to zero and G_N converges to the aleatoric component $\frac{1}{2} \log(2\pi e \sigma_{\text{true}}^2)$, i.e., if $\mu_{\text{pred}} = \mu_{\text{true}}$ and $\sigma_{\text{pred}}^2 = \sigma_{\text{true}}^2$ then $\text{KL} \left[\mathcal{N}(y | \mu_{\text{true}}, \sigma_{\text{true}}^2) || \mathcal{N}(y | \mu_{\text{pred}}, \sigma_{\text{pred}}^2) \right] = 0$.

A.2.1. ASYMPTOTIC BEHAVIORS

In [Watanabe \(1999\)](#); [Hay \(2025\)](#) it's showed that the generalization error and the free energy have the following asymptotic expansions:

$$\mathbb{E}_n[G_N] = \frac{\lambda}{n} - \frac{m-1}{n \log n} + o\left(\frac{1}{n \log n}\right) \quad (39)$$

$$F_N = nS_n + \lambda \log n - (m-1) \log \log n + O_p(1) \quad (40)$$

where λ is a positive rational number, m a positive integer and $\mathbb{E}_n[\cdot]$ is the expectation operator the overall dataset. The constant λ is called the RLCT or learning coefficient, since it is dominant in the leading terms of the equations above, which represents the $\mathbb{E}_n[G_n] - n$ and $F_n - n$ learning curves. In algebraic geometry, m is called a multiplicity. In the case of regular models $\lambda = \frac{d}{2}$ and $m = 1$, where d is the number of model parameters.

A.2.2. ON CONNECTING SLT TO UNCERTAINTY SCALING IN DEEP MODELS

Our use of Bayesian linear regression is primarily to illustrate how, in a simplified setting, generalization error can be cleanly decomposed into aleatoric and epistemic components, thereby exposing uncertainty measures that are otherwise less apparent. We are aware that this only scrapes the surface of the problem, as extending these insights to deep, over-parameterized networks remains an open challenge. Within the broader perspective of SLT ([Watanabe, 2009](#)), neural networks form a singular and non-realizable class of models, for which theoretical results—such as asymptotic error bounds or explicit learning coefficients—are scarce. In particular, Bayes and Gibbs errors are governed by the RLCT, which quantifies effective dimensionality; yet for over-parameterized architectures, the roles of RLCT and related invariants remain poorly understood despite recent advances in local approximations, such as the Local Learning Coefficient (LLC) ([Lau et al., 2024](#)).

B. Uncertainty scaling: a study on linearized Laplace

B.1. Setup

We consider a classification problem with C classes on a dataset $\mathcal{D} = \{(\mathbf{x}_n, y_n)\}_{n=1}^N$, where inputs $\mathbf{x}_n \in \mathbb{R}^D$ and targets $y_n \in \{1, \dots, C\}$. The model is a Bayesian neural network (BNN) with parameters $\boldsymbol{\theta} \in \mathbb{R}^P$ mapping inputs to a vector of logits $\mathbf{f}(\mathbf{x}; \boldsymbol{\theta}) \in \mathbb{R}^C$. The likelihood is defined as $p(\mathcal{D} | \boldsymbol{\theta}) = \prod_{n=1}^N p(y_n | \mathbf{f}(\mathbf{x}_n; \boldsymbol{\theta}))$. The log-joint density (unnormalized posterior) can be written as:

$$\ell(\boldsymbol{\theta}, \mathcal{D}) = \sum_{n=1}^N \log p(y_n | \mathbf{f}(\mathbf{x}_n; \boldsymbol{\theta})) + \log p(\boldsymbol{\theta}). \quad (41)$$

The Laplace approximation constructs a Gaussian surrogate $q(\boldsymbol{\theta}) \approx p(\boldsymbol{\theta} | \mathcal{D})$ by matching the curvature of the true posterior at its peak. This is achieved via a second-order Taylor expansion of $\ell(\boldsymbol{\theta}, \mathcal{D})$ around the maximum a posteriori (Maximum a posteriori (MAP)) estimate $\boldsymbol{\theta}_{\text{MAP}}$:

$$\ell(\boldsymbol{\theta}, \mathcal{D}) \approx \ell(\boldsymbol{\theta}_{\text{MAP}}, \mathcal{D}) + \underbrace{\nabla \ell(\boldsymbol{\theta}_{\text{MAP}})}_{=0}^\top (\boldsymbol{\theta} - \boldsymbol{\theta}_{\text{MAP}}) + \frac{1}{2} (\boldsymbol{\theta} - \boldsymbol{\theta}_{\text{MAP}})^\top \nabla^2 \ell(\boldsymbol{\theta}_{\text{MAP}}) (\boldsymbol{\theta} - \boldsymbol{\theta}_{\text{MAP}}). \quad (42)$$

Since $\boldsymbol{\theta}_{\text{MAP}}$ is a local maximum, the gradient term vanishes. Identifying the remaining quadratic form with the log-density of a Gaussian $\mathcal{N}(\boldsymbol{\theta}_{\text{MAP}}, \boldsymbol{\Sigma})$ yields the approximation parameters:

$$q(\boldsymbol{\theta}) = \mathcal{N}(\boldsymbol{\theta}_{\text{MAP}}, \boldsymbol{\Sigma}), \quad (43)$$

$$\boldsymbol{\theta}_{\text{MAP}} = \arg \max_{\boldsymbol{\theta}} \ell(\boldsymbol{\theta}, \mathcal{D}), \quad (44)$$

$$\boldsymbol{\Sigma} = - \left[\nabla_{\boldsymbol{\theta}\boldsymbol{\theta}}^2 \ell(\boldsymbol{\theta}, \mathcal{D}) \Big|_{\boldsymbol{\theta}=\boldsymbol{\theta}_{\text{MAP}}} \right]^{-1}, \quad (45)$$

where the covariance $\boldsymbol{\Sigma}$ is defined as the negative inverse Hessian.

However, computing the full Hessian is unfeasible in practice. The Generalized Gauss-Newton (GGN) approximation is commonly adopted for tractability. Under the GGN, the per-data-point Hessian is approximated using the Fisher Information:

$$\nabla_{\boldsymbol{\theta}\boldsymbol{\theta}}^2 \log p(y | \mathbf{f}(\mathbf{x}; \boldsymbol{\theta})) \approx -J_{\boldsymbol{\theta}}(\mathbf{x})^{\top} \boldsymbol{\Lambda}(\mathbf{f}) J_{\boldsymbol{\theta}}(\mathbf{x}), \quad (46)$$

where $\boldsymbol{\Lambda}(\mathbf{f}) = -\mathbb{E}_{y \sim p(y|\mathbf{f})} [\nabla_{\mathbf{f}\mathbf{f}}^2 \log p(y|\mathbf{f})] \in \mathbb{R}^{C \times C}$ is the Hessian of the negative log-likelihood w.r.t the logits (which coincides with the Fisher information metric for canonical link functions), and $J_{\boldsymbol{\theta}}(\mathbf{x}) \in \mathbb{R}^{C \times P}$ is the Jacobian of the outputs w.r.t the parameters.

Following Immer et al. (2021), the GGN approximation enables a local linearization of the network $f_{\boldsymbol{\theta}}(\mathbf{x})$ around $\boldsymbol{\theta}^*$ (usually taken as $\boldsymbol{\theta}_{\text{MAP}}$):

$$\mathbf{f}_{\text{lin}}^{\boldsymbol{\theta}^*}(\mathbf{x}; \boldsymbol{\theta}) = \mathbf{f}(\mathbf{x}; \boldsymbol{\theta}^*) + J_{\boldsymbol{\theta}^*}(\mathbf{x})(\boldsymbol{\theta} - \boldsymbol{\theta}^*). \quad (47)$$

This reduces the BNN to a multi-output Generalized linear model (GLM). Comparing the two predictive distributions:

$$p_{\text{BNN}}(y | \mathbf{x}, \mathcal{D}) = \mathbb{E}_{q(\boldsymbol{\theta})} [p(y | \mathbf{f}(\mathbf{x}; \boldsymbol{\theta}))], \quad (48)$$

$$p_{\text{GLM}}(y | \mathbf{x}, \mathcal{D}) = \mathbb{E}_{q(\boldsymbol{\theta})} [p(y | \mathbf{f}_{\text{lin}}^{\boldsymbol{\theta}^*}(\mathbf{x}; \boldsymbol{\theta}))]. \quad (49)$$

Notably, p_{GLM} pushes the posterior Gaussian through the linearized function, resulting in a Gaussian distribution in logit space, while p_{BNN} uses the original non-linear network.

B.2. Uncertainty quantification

To decompose the uncertainty we use the law of total variance on the one-hot encoded target variable \mathbf{y}^* . Considering a test point \mathbf{x}^* , the predictive covariance (TU) is:

$$\mathbb{V}[\mathbf{y}^* | \mathbf{x}^*, \mathcal{D}] = \underbrace{\mathbb{E}_{q(\boldsymbol{\theta})} [\mathbb{V}[\mathbf{y}^* | \mathbf{x}^*, \boldsymbol{\theta}]]}_{\text{AU}} + \underbrace{\mathbb{V}_{q(\boldsymbol{\theta})} [\mathbb{E}[\mathbf{y}^* | \mathbf{x}^*, \boldsymbol{\theta}]]}_{\text{EU}}, \quad (50)$$

where $\mathbb{E}[\mathbf{y}^* | \mathbf{x}^*, \boldsymbol{\theta}] = \text{softmax}(\mathbf{f}(\mathbf{x}^*; \boldsymbol{\theta}))$ corresponds to the model's output probabilities. Both AU and EU are $C \times C$ positive semi-definite matrices.

- The AU matrix captures the expected inherent noise (irreducible aleatoric uncertainty).
- The EU matrix captures the model's uncertainty regarding the true class probabilities (epistemic uncertainty).

To make the computation explicit, we assume an isotropic Gaussian prior $p(\boldsymbol{\theta}) = \mathcal{N}(\boldsymbol{\theta}; \mathbf{0}, \lambda^{-1}\mathbf{I})$, implying $\nabla_{\boldsymbol{\theta}\boldsymbol{\theta}}^2 \log p(\boldsymbol{\theta}) = -\lambda\mathbf{I}$. Consequently, the posterior covariance $\boldsymbol{\Sigma}$ is determined by the sum of the data-induced curvature (Fisher information) and the prior precision:

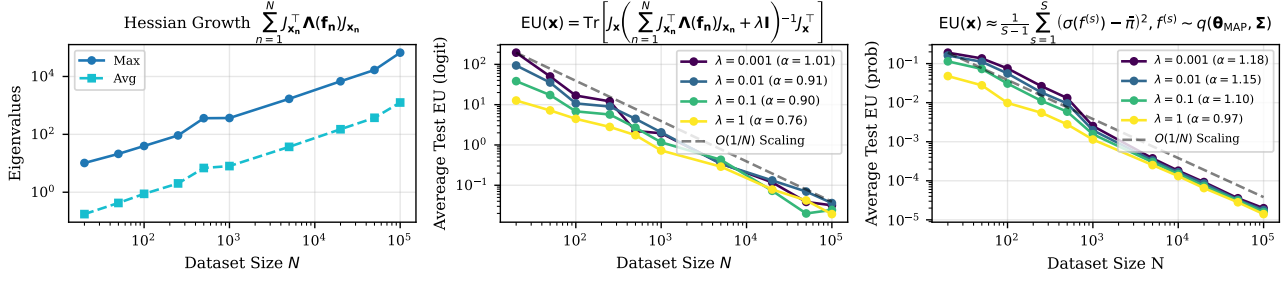


Figure 12. **Scaling Analysis of LLA:** (Left) Growth of the Hessian (data precision) spectrum as a function of dataset size N . Both the maximum eigenvalue (blue) and the average eigenvalue (cyan) scale linearly with N , confirming that information accumulates additively. (Right) Average EU on the test set for varying prior precisions $\lambda \in [0.001, 1]$. The dashed (gray) line indicates the theoretical $O(N^{-1})$ reference scaling. The legend displays the empirical scaling exponent α for each prior setting (where $\text{EU} \propto N^{-\alpha}$), showing that all curves asymptotically converge to the data-driven N^{-1} regime regardless of the prior strength.

$$\Sigma = \left(\sum_{n=1}^N J_{\mathbf{x}_n}^\top \mathbf{\Lambda}(\mathbf{f}_n) J_{\mathbf{x}_n} + \lambda \mathbf{I} \right)^{-1}. \quad (51)$$

We study the predictive covariance in logit space, which serves as a proxy for the EU in probability space of Equation (50). Using the linearized predictive p_{GLM} , the covariance matrix is given by:

$$\Sigma_{\text{logit}}(\mathbf{x}) = \mathbb{V}_{q(\boldsymbol{\theta})}[\mathbf{f}_{\text{lin}}^{\boldsymbol{\theta}^*}(\mathbf{x}; \boldsymbol{\theta})] \quad (52)$$

$$= \mathbb{V}[\mathbf{f}(\mathbf{x}; \boldsymbol{\theta}^*) + J_{\mathbf{x}}(\boldsymbol{\theta} - \boldsymbol{\theta}^*)] \quad (53)$$

$$= J_{\mathbf{x}} \mathbb{V}[\boldsymbol{\theta}] J_{\mathbf{x}}^\top \quad (54)$$

$$= J_{\mathbf{x}} \Sigma J_{\mathbf{x}}^\top \quad (55)$$

$$= J_{\mathbf{x}} \left(\sum_{n=1}^N J_{\mathbf{x}_n}^\top \mathbf{\Lambda}(\mathbf{f}_n) J_{\mathbf{x}_n} + \lambda \mathbf{I} \right)^{-1} J_{\mathbf{x}}^\top \in \mathbb{R}^{C \times C}. \quad (56)$$

The scalar epistemic uncertainty is obtained by taking the trace of this covariance matrix (summing the variances across output dimensions):

$$\text{EU}_{\text{logit}}(\mathbf{x}) = \text{Tr}(\Sigma_{\text{logit}}(\mathbf{x})). \quad (57)$$

The term $J_{\mathbf{x}_n}^\top \mathbf{\Lambda}(\mathbf{f}_n) J_{\mathbf{x}_n}$ represents the precision contributed by the training data. If the test Jacobian $J_{\mathbf{x}}$ is orthogonal to the subspace spanned by the training gradients, the covariance reduces to the prior term $\lambda^{-1} J_{\mathbf{x}} J_{\mathbf{x}}^\top$.

As highlighted by Immer et al. (2021), the Bayesian GLM in weight space is equivalent to a GP in function space with a particular kernel.

B.3. Experiments: shallow models

Dataset. We use the Two Moons dataset, a binary classification problem ($C = 2$) with inputs $\mathbf{x} \in \mathbb{R}^2$. To observe the transition from the prior-dominated to the data-dominated regime, we generated training sets of varying sizes $N \in \{5, 10, 20, 50, 100, 200, 500\}$. A fixed independent test set of $N_{\text{test}} = 100$ samples was used for evaluation.

Model Architecture. We employed an MLP with a single hidden layer and tanh activation functions. The default architecture consisted of 50 hidden units. The model parameters MAP were estimated via standard regularized cross-entropy minimization using the Adam optimizer. All experiments were repeated over 3 independent folds with different random seeds for data generation and weight initialization.

We computed the uncertainty using the Linearized Laplace approximation (GLM predictive):

1. **Hessian Approximation:** We use the GGN approximation to the Hessian and computed the *full* Hessian covariance matrix $\Sigma \in \mathbb{R}^{P \times P}$ (where P is the number of parameters).
2. **Linearization:** The predictive distribution was treated as a GLM by linearizing the network function around the MAP estimate.
3. **Prior:** We train models with different prior’s precision λ to observe the shift in the "knee" of the scaling curve (the transition from prior to data dominance).
4. **Uncertainty Metrics:** We quantify EU using two complementary metrics to capture uncertainty in both function and probability space:

- **Variance (logit space):** For a given test point \mathbf{x} , we compute the trace of the predictive covariance in logit space. This serves as a proxy for the volume of the posterior in function space:

$$\text{EU}_{\text{logit}}(\mathbf{x}) = \mathbb{V}_{q(\boldsymbol{\theta})}[\mathbf{f}_{\text{lin}}^{\boldsymbol{\theta}^*}(\mathbf{x}; \boldsymbol{\theta})] \quad (58)$$

$$= \text{Tr}(J_{\mathbf{x}} \Sigma J_{\mathbf{x}}^{\top}), \quad (59)$$

where $J_{\mathbf{x}} \in \mathbb{R}^{C \times P}$ is the Jacobian of the model output w.r.t parameters.

Theoretical expectations: Assuming the training data is i.i.d., the accumulated Fisher information grows linearly with N . Consequently, in the data-dominated regime (large N), the posterior variance scales as $\Sigma_N \propto \frac{1}{N}$. See Figure 12.

- **Variance (probability space):** In the binary setting, this metric captures the variance of the predicted Bernoulli parameter $\pi = \sigma(f)$ induced by the posterior on the weights. Since the mapping from logit space to probability space is non-linear, a Gaussian distribution on f does not result in a Gaussian on π . The variance is given by:

$$\text{EU}_{\text{var}}(\mathbf{x}) = \mathbb{V}_{q(\boldsymbol{\theta})} \left[\sigma(f_{\text{lin}}^{\boldsymbol{\theta}^*}(\mathbf{x}; \boldsymbol{\theta})) \right]. \quad (60)$$

Unlike the logit-space variance, this quantity is bounded in $[0, 0.25]$. Because the sigmoid saturates, high variance in logit space does not necessarily translate to high variance in probability space if the mean is far from the decision boundary. This expectation is typically intractable and is approximated via Monte Carlo sampling using S samples from $q(\boldsymbol{\theta})$:

$$\text{EU}_{\text{var}}(\mathbf{x}) \approx \frac{1}{S-1} \sum_{s=1}^S \left(\sigma(f^{(s)}) - \bar{\pi} \right)^2, \quad \text{where } f^{(s)} \sim q(\boldsymbol{\theta}_{\text{MAP}}, \Sigma). \quad (61)$$

Theoretical expectations: Applying the Delta method (first-order Taylor expansion) to the sigmoid function, the variance in probability space is approximated by:

$$\mathbb{V}[\sigma(f)] \approx \left[\frac{\partial \sigma(f)}{\partial f} \right]^2 \mathbb{V}[f] = \left[\pi(1 - \pi) \right]^2 \cdot \text{EU}_{\text{logit}}(\mathbf{x}). \quad (62)$$

While the asymptotic rate remains $O(N^{-1})$, the magnitude is heavily dampened by the term $[\pi(1 - \pi)]^2$. As the model becomes more confident (predictions π close to 0 or 1), the gradient of the sigmoid vanishes, suppressing the visible EU even if the underlying logit uncertainty is moderate.

- **Entropy (probability space):** We also measure the EU in probability space via the Mutual Information (MI) between predictions and parameters. This is estimated using Monte Carlo sampling with S samples from the GLM predictive:

$$\text{EU}_{\text{ent}}(\mathbf{x}) = H \left[\frac{1}{S} \sum_{s=1}^S \mathbf{p}_s \right] - \frac{1}{S} \sum_{s=1}^S H[\mathbf{p}_s], \quad (63)$$

where $H[\cdot]$ denotes the Shannon entropy, $\mathbf{p}_s = \text{softmax}(\mathbf{f}_{\text{lin}}^{\boldsymbol{\theta}^*}(\mathbf{x}; \boldsymbol{\theta}_s))$, and $\boldsymbol{\theta}_s \sim \mathcal{N}(\boldsymbol{\theta}_{\text{MAP}}, \Sigma)$.

Theoretical expectations: Similar to the variance metric, the MI scales asymptotically as $O(N^{-1})$. By applying a second-order Taylor expansion to the entropy functional around the mean prediction $\bar{\mathbf{p}}$, the MI can be approximated as:

$$\text{EU}_{\text{ent}}(\mathbf{x}) \approx \frac{1}{2} \text{Tr} (\mathcal{I}(\bar{\mathbf{p}}) \cdot \mathbb{V}[\mathbf{p}]), \quad (64)$$

where $\mathcal{I}(\bar{\mathbf{p}})$ is the Fisher Information of the observation model evaluated at the mean prediction. Since the predictive variance $\mathbb{V}[\mathbf{p}]$ is driven by the posterior weight variance $\Sigma \propto N^{-1}$, the entropy-based uncertainty inherits this scaling, converging linearly to zero in the large data limit.

C. Additional results

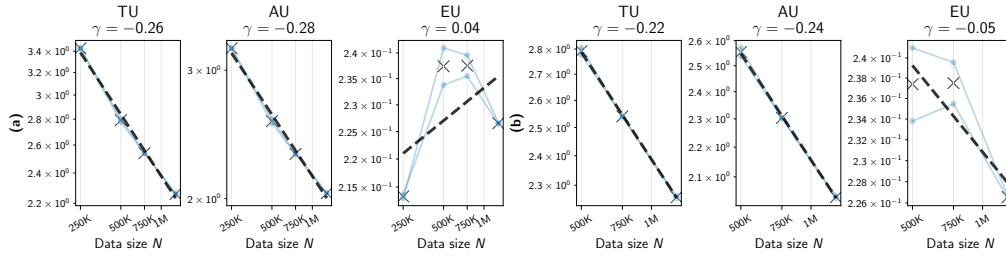


Figure 13. **Vision Transformer (ViT) on ImageNet-32 dataset:** We use MCD with fixed dropout rate $p = 0.1$. We train for 200 epochs using SGD with cosine annealing. In (a) we report uncertainty scaling on subsets from size 250K up to 1.2M. In (b) we discard the first point highlighting the decreasing rate of EU for large values of N .

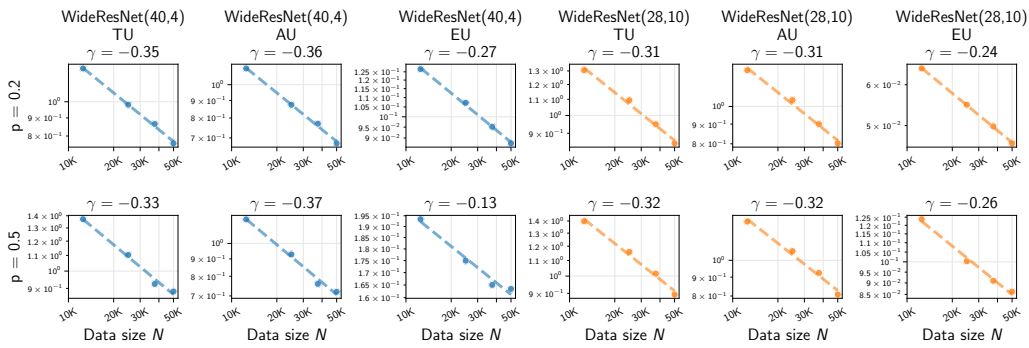


Figure 14. **WideResNets (w,d) on CIFAR-100 dataset:** We train the models with MCD with fixed dropout rate $p = 0.2$ (first row) and $p = 0.5$ (second row). We consider 25%, 50%, 75% and 100% subsets of the training data and we show the mean uncertainty for each N subset. Dashed lines represent linear regression fitted to the test mean of each uncertainty metric. Both axes are on a logarithmic scale.

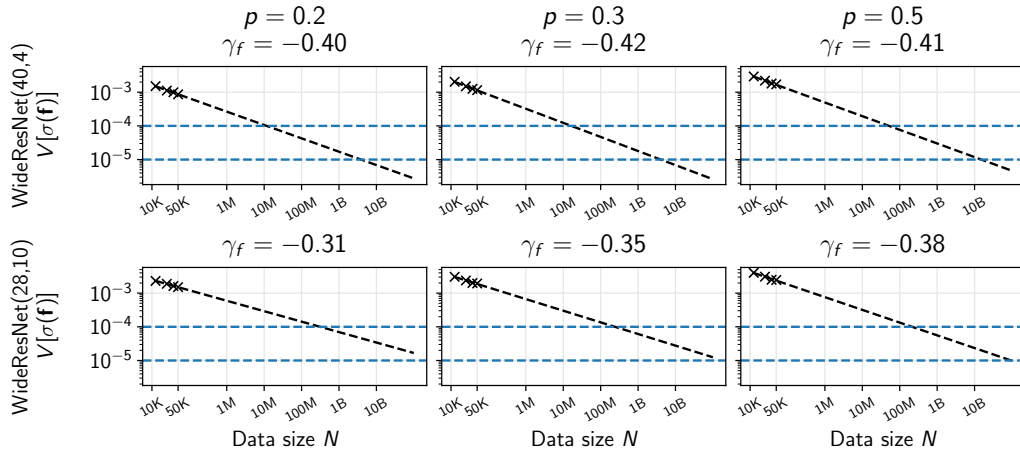


Figure 15. **WideResNets (w,d) on CIFAR-10 dataset - extrapolation:** We report uncertainty trends for different WideResNets and dropout rates. We mention in the main paper that the scaling laws we derive in this context are practically useful to extrapolate uncertainties to N arbitrarily large. We report $\mathbb{V}[\sigma(\mathbf{f})]$, the variance computed over the Softmax predictions of the Monte Carlo (MC) samples, averaged over all the test samples (\times in the plots). The black dashed lines have slope γ_f , the blue dashed lines correspond to two thresholds of predictive uncertainty.

Scaling Laws for Uncertainty in Deep Learning

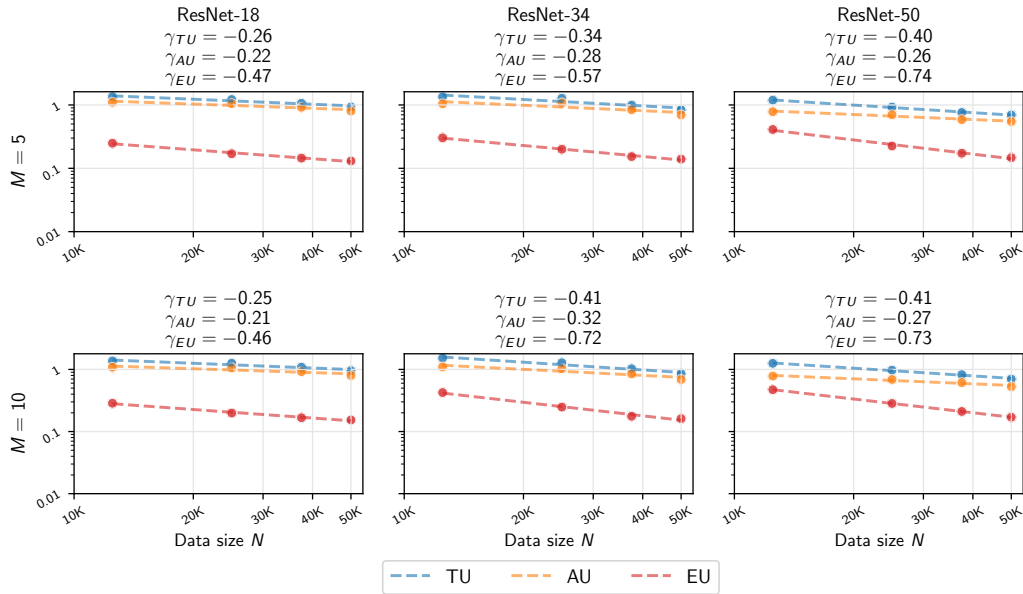


Figure 16. **ResNets on CIFAR-100 dataset with DE:** We train the models with DE with ensemble members $M = 5$ (first row) and $M = 10$ (second row). We consider 25%, 50%, 75% and 100% subsets of the training data and we show the mean uncertainty for each N subset. Dashed lines represent linear regression fitted to the test mean of each uncertainty metric. Both axes are shown on a logarithmic scale.

Scaling Laws for Uncertainty in Deep Learning

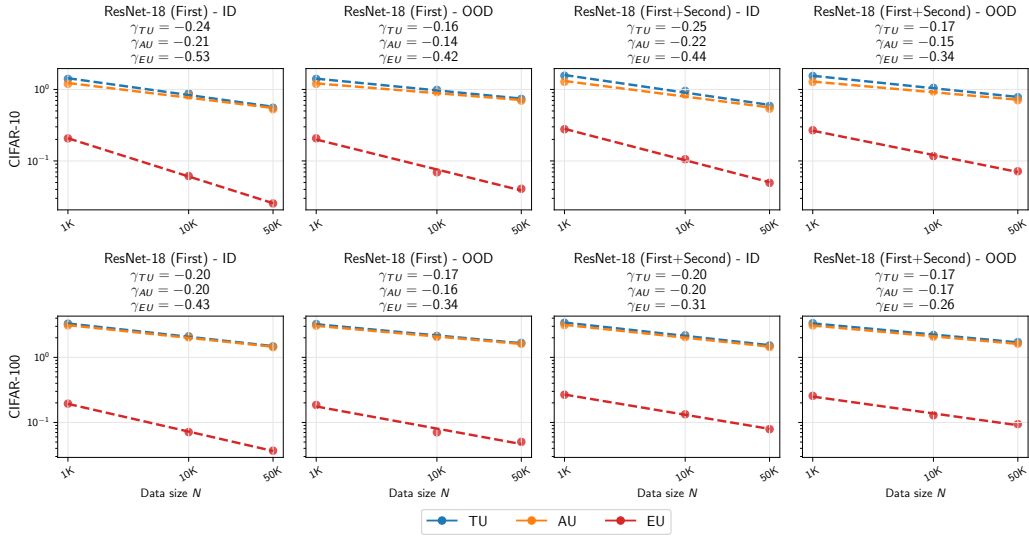


Figure 17. **ResNet-18 on CIFAR-10 and CIFAR-100 datasets with MCMC:** We report uncertainties obtained through MCMC considering only the first layer stochastic (First) and only the first two layers stochastic (First+Second). We show the scaling for both in-distribution (ID) and out-of-distribution (OOD) predictive uncertainties. On the first row the mean uncertainty scaling for CIFAR-10 using CIFAR-10-C as OOD dataset while on the second row the mean uncertainty scaling for CIFAR-100 using CIFAR-100-C as OOD dataset.

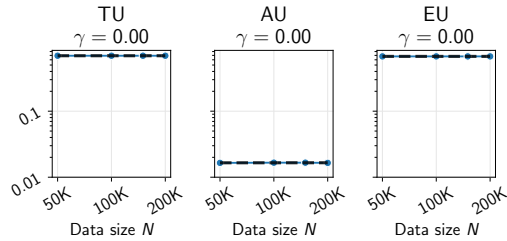


Figure 18. **Uncertainty scaling with Bayesian LoRA:** For completeness, we report the uncertainty scaling we get when fine-tuning LLM Phi on Quora Questions Pairs (qqp) dataset using increasing training subsets and by doing Laplace approximation over the LoRA parameters following Yang et al. (2024). These curves are completely flat, suggesting that assessing predictive uncertainty on much smaller (fine-tuning) data compared to the massive amount used for pre-training doesn't give any insight about the scaling laws of the metrics of interest.

D. Experimental setup

Table 1. Vision Transformer (ViT) architecture: To obtain the results in Figure 8 and Figure 13, we use a compact ViT model with details specified in the table below. The implementation is available at <https://github.com/kentaroy47/vision-transformers-cifar10>.

Parameter	Value
Patch size	4
Embedding dimension	512
Transformer depth	6
Number of attention heads	8
MLP hidden dimension	512

Table 2. Algorithmic dataset: To obtain the results in Figure 10 we use a GPT-2 model and train it for 10,000 epochs with AdamW (Loshchilov & Hutter, 2019) optimizer (learning rate 10^{-4}) and linear scheduler with 100 warmup steps. Implementation available at <https://github.com/openai/grok/tree/main/scripts>.

Parameter	Value
Max sequence length	256
Embedding size	128
Number of layers	2
Number of attention heads	4
Dropout (residuals)	0.1
Dropout (embeddings)	0.1
Dropout (attention)	0.1

Table 3. IVON configuration and training setup: To obtain the results in Figure 7 we follow the setup of Shen et al. (2024) for image classification. The optimizer is combined with a scheduler (initial linear warm-up followed by cosine annealing). In this table we report the hyper-parameters we set following the same notation of Shen et al. (2024) and of the official implementation available at <https://github.com/team-approx-bayes/ivon>.

Parameter	Value
Total epochs	200
Warm-up epochs	5
Batch size	50
Initial learning rate	2.5
β_1	0.9
β_2	$1 - 5 \times 10^{-6}$
Weight decay	5×10^{-5}
Hessian init	0.05
ESS λ	1,281,167
N	1,281,167
MC test samples	10